Renewable Energy 168 (2021) 960–971

Contents lists available at ScienceDirect

Renewable Energy

journal homepage: www.elsevier.com/locate/renene

Numerical study of turbulent flow past a rotating axial-flow pump based on a level-set immersed boundary method

Kan Kan [a, e, *], Zixuan Yang [b, c, **], Pin Lyu [d, e], Yuan Zheng [a], Lian Shen [e]

[a] College of Energy and Electrical Engineering, Hohai University, Nanjing, 211100, China
[b] Institute of Mechanics, Chinese Academy of Sciences, Beijing, 100864, China
[c] School of Engineering Sciences, University of Chinese Academy of Sciences, Beijing, 100049, China
[d] Key Lab of Structures Dynamic Behavior and Control of the Ministry of Education, Harbin Institute of Technology, Harbin, 150090, China
[e] Department of Mechanical Engineering and Saint Anthony Falls Laboratory, University of Minnesota, Minneapolis, MN, 55455, USA

ARTICLE INFO

Article history:
Received 23 June 2020
Received in revised form
23 December 2020
Accepted 24 December 2020
Available online 29 December 2020

Keywords:
Axial-flow pump
Large-eddy simulation
Immersed boundary method
Level set function
Turbulent kinetic energy
Flow separation

ABSTRACT

Large-eddy simulation is performed to study the turbulence statistics and flow structures of the water past a rotating axial-flow pump under different flow-rate working conditions. A novel sharp-interface level-set based immersed boundary method is applied to capture the complex geometry of the pump. An unstructured triangular mesh is used to discretize the complex surface geometry of the pump, and a ray-tracing method is employed to classify the computational domain into fluid and solid regions. Turbulence statistics, including the mean velocity, turbulent kinetic energy (TKE), turbulence production, and turbulence dissipation, are analyzed under five different flow-rate working conditions around the designed condition. The results show that unsteady wake, tip leakage flow, and flow separation are accompanied by a high TKE magnitude. For the high turbulence intensity under off-designed working conditions, the tip leakage flow plays a leading role at low flow-rates, and flow separation dominates at high flow-rates.

1. Introduction

Pumps are used to drive fluid flows in various applications over a wide range of physical scales, from blood vessels to pumping stations [1,2]. At large scales, the pump unit is the core component in pumping stations to prevent or control floods, and to irrigate, transfer, and supply water resources. The present study focuses on axial-flow pumps, which are usually used in applications with high flow-rates and low lifted fluid heads. The investigation of flow past an axial-flow pump is challenging because of the complex geometries and the highly turbulent motions.

In the research of axial-flow pump, Zierke et al. [3–5] utilized a high Reynolds number pump (HIREP) facility to investigate the flow. Their experiments generated a large amount of data, including information about the pressure over the surface, flow structures, and exit flow of the static inlet guide vanes. They also provided extensive results of the flow characteristics around rotating impeller blades, including the static-pressure distribution, surface flow visualization, exit flow, tip leakage vortex, and integral quantities including shaft thrust and torque. Uzol et al. [6] designed a facility that overcomes optical obstructions to the illuminating sheet and camera caused by the blade, and performed particle image velocimetry (PIV) measurements of the flow field around an axial turbo-pump. They investigated the instantaneous and phase-averaged flow quantities around the blades, and showed detailed velocity distribution in the boundary layer and near wake. They found that the rotor–stator interaction (RSI) contributed mostly to the generation of high stresses near the blades and in the wake. Zhang et al. [7] and Tan et al. [8,9] studied the tip leakage vortex (TLV) of axial and mixed flow pumps also by means of experiments and simulations, which revealed the characteristics of vortex structures, turbulence statistics, and tip-attached cavitations. Song and Liu [10] investigated the pressure pulsation induced by floor-attached vortex at the bottom of an axial-flow pump sump through experiment, which revealed the law of pressure pulsation under the complex vortex effect.

While it is challenging to measure the unsteady flows in axial-

* Corresponding author. College of Energy and Electrical Engineering, Hohai University, Nanjing, 211100, China.
** Corresponding author. Institute of Mechanics, Chinese Academy of Sciences, Beijing, 100864, China.
E-mail addresses: kankan@hhu.edu.cn (K. Kan), yangzx@imech.ac.cn (Z. Yang).

https://doi.org/10.1016/j.renene.2020.12.103
0960-1481/

flow pumps with complex geometries in experiments, obtaining accurate and detailed descriptions of the flow field through numerical simulation is also highly critical, in the context of unsteady Reynolds-averaged Navier-Stokes equations (RANS) and large-eddy simulation (LES) methods. The unsteady RANS method with various turbulence models has been used to study the flow characteristics in turbo machinery over the past few decades. Muggli et al. [11] studied the behavior of the flow in a mixed flow pump using RANS with a standard k-ε turbulence model. Liu et al. [12,13] developed a very high-efficient axial-flow pump system and studied the flow characteristics with a RNG k-ε turbulence model. Although some studies applied the shear stress transport (SST) turbulence model, declaring an improvement on the prediction of flow separation in the numerical studies of flow dynamics past a pump [14–18], RANS occasionally fails in predicting separation and capturing the highly complex turbulent flow physics [19,20]. Therefore, applying LES is desirable for the turbomachinery applications with intense turbulent motions. Because of the high computational cost, LES results about such flows are sparse. Byskov et al. [21] conducted LES of a centrifugal pump impeller and validated the mean velocity against RANS and experimental results. The comparison showed that the LES results were in better agreement with experimental results than the RANS results. Kato et al. [22] developed an overset finite-element LES method to simulate a high-specific-speed mixed-flow pump, and Yamade et al. [23] validated the prediction performance of a mixed-flow pump by LES and analyzed the instability characteristics.

The above simulation studies are based on body-fitted grid. In the conventional arbitrary Lagrangian-Eulerian (ALE) method, it is challenging to generate mesh over the complex geometry of the pump. Meanwhile, as the greatest limitation of employing body-fitted grids to the moving boundaries, it is computationally expensive to handle large movements and deformations of structures, such as the guide vane adjustment in hydraulic turbines [24–27]. Although the immersed boundary (IB) method is convenient for capturing complex boundary geometries, few applications to complex machinery exist in the literature. Kang et al. [28] studied the three dimensional (3D) wake structure of a hydrokinetic turbine based on the IB method. Angelidis et al. [29] incorporated an adaptive mesh refinement technology to conduct a geometry-resolving LES of the flow past a hydrokinetic turbine. Chawdhary et al. [30] studied an array of hydrokinetic turbines in a field-scale river environment with a multi-resolution LES. Posa et al. [20] conducted LES for geometrically complex mixed-flow pumps using the IB method. These LES studies of the flows past turbine or pumps mainly focused on the large-scale flow structures in the wake, while the flow details around the turbine or pump were not the focus due to the limitation in the computer power.

In this paper, we extend the IB method algorithm [31] to simulate the fluid-structure interaction (FSI) problems between fluids and arbitrary complex bodies. An unstructured mesh is utilized to discretize the complex solid bodies [32]. A ray-tracing method is utilized to classify the fluid and solid computational nodes [33,34]. The above methods are applied to study LES of a complex axial-flow pump with fully developed turbulence inflow conditions to reveal the characteristics of the turbulence statistics and vortex structures in the pump. While the RANS method may make reasonable predictions on the mean flow by adjusting the parameter values in turbulence models based on the experience of users, the LES method can provide more accurate results of instantaneous flow field and turbulent structures without artificial inference with the model parameters. Meanwhile, the present study provides insights into the flow physics by analyzing turbulence statistics, including the turbulent kinetic energy (TKE), TKE production and dissipation. To our best knowledge, the present study is the first LES investigation on the detailed flow structures in the vicinity of the pump components under various flow-rate working conditions.

The remainder of this paper is organized as follows: In Section 2, the numerical method is described. In Section 3, the setup of the simulation of the flow past an axial-flow pump is introduced. In Section 4, a comparative study of the turbulent flow of an axial-flow pump under five different flow-rate working conditions is conducted, with conclusions given in section 5.

2. Simulation method

2.1. Governing equations and boundary conditions

The LES is governed by the filtered Navier–Stokes equations for incompressible flow as follows:

$$\nabla \cdot \boldsymbol{u} = 0, \tag{1}$$

$$\frac{\partial \boldsymbol{u}}{\partial t} + \boldsymbol{u}\cdot\nabla\boldsymbol{u} = \frac{1}{\rho}\left(-\nabla p + \nabla\cdot(\mu \boldsymbol{S}) + \rho \boldsymbol{g} - \nabla\cdot\boldsymbol{\tau}_{sgs}\right). \tag{2}$$

Here, $\boldsymbol{u}$ is the filtered velocity vector, t is the physical time, ρ is the fluid density, p is the pressure, μ is the fluid dynamic viscosity, S is the strain-rate tensor based on u, g is the gravitational acceleration, and $\boldsymbol{\tau}_{sgs}$ is the subgrid-scale (SGS) stress tensor, calculated using the dynamic Smagorinsky model [35–37].

Assuming that $\boldsymbol{l}(t)$ is the position vector of an arbitrary point located on the immersed boundaries of solid bodies at one time instant, the velocity of the same point in the fluid field $\boldsymbol{u}(t)$ satisfies the no-slip boundary conditions:

$$\boldsymbol{u}(t) = \frac{\partial \boldsymbol{l}(t)}{\partial t}. \tag{3}$$

Specifically, when $\boldsymbol{l}(t)$ is located on a stationary boundary, $\boldsymbol{u}(t)$ is equal to 0. The Neumann boundary condition for pressure comes from projecting the momentum equation (2) to the immersed boundaries in the normal direction:

$$-\frac{\mathrm{d}p}{\mathrm{d}\boldsymbol{n}} = \rho \boldsymbol{n}\cdot\left(\frac{\mathrm{D}\boldsymbol{u}}{\mathrm{D}t} + \boldsymbol{g} - \nu\nabla^2\boldsymbol{u}\right), \tag{4}$$

where $\boldsymbol{n}_w$ is the wall normal vector and $\nu = \mu/\rho$ is the fluid kinematic viscosity.

2.2. Numerical schemes

The governing equations are discretized using the finite difference method. Based on the staggered grid, the pressure is defined at cell centers, and the three orthogonal components of the velocity are placed at the centers of the cell faces. The momentum equations are integrated in time using the second-order Runge–Kutta (RK2) method. The divergence-free condition is satisfied using the projection method. A dynamic time step calculated based on the CFL number was used during the simulation. The Portable, Extensible Toolkit for Scientific Computation (PETSc) and parallel computing by message passing interface (MPI) library are utilized to solve the Poisson equation and for parallel computing, respectively. PETSc is a suite of data structures and routines for the scalable (parallel) solution of scientific applications modeled by partial differential equations [38]. The code is developed in house. More details about our numerical code and its validations can be found in previous papers [31,39–41].

2.3. LS-based IB method and reconstruction of the velocity field

In our IB scheme, a level-set (LS) function that represents the signed distance value from the solid boundary needs to be assigned at each Cartesian grid node. In the previous method of Cui et al. [31], analytic functions are adopted to calculate the distance values from the grid nodes to the boundaries. Then positive and negative signs are used to distinguish the fluid and solid domains, respectively. The interface is captured by a linear interpolation of grid nodes located on the two sides of and immediately vicinal to the fluid-solid interface, which is the isosurface of the LS function equal to 0.

For a two dimensional (2D) case, in Fig. 1, the location of the projected node from the IB point in the interface normal direction is obtained by a linear interpolation from the LS function values on the nodes closest to the fluid-solid interface. Meanwhile, with two fluid nodes (three nodes in 3D cases) and the projected node on the interface, the velocity at IB nodes is reconstructed by interpolations to satisfy the no-slip boundary conditions. The gray domain shown is the solid domain, which is excluded from the computation. The velocities of projected nodes at interface and nodes in the solid domain depend on the motion of the solid bodies. Particularly, the velocity is zero while solid body is stationary. The pressure boundary conditions of equation (4) are applied at the interface of the fluid domain and solid domain when solving the Poisson equation. More details about the IB method are introduced in previous papers [31,40,41].

Different from the previous method of Cui et al. [31], which used a linear interpolation, a logarithmic wall-layer model is applied in the present cases at high Reynolds numbers [42]. The tangential velocity satisfies the law of the wall as follows:

$$\frac{u_t}{u_\tau} = \frac{1}{\kappa}\ln(y^+) + B, \tag{5}$$

where u_t is the tangential velocity, u_τ is the local instantaneous friction velocity, κ is the von Kármán constant and equal to 0.41, y^+ is the non-dimensional distance to the wall, and B is a constant and equal to 5.5. Because y^+ differs at different IB nodes, the tangential velocity at an IB node is calculated when the IB node is located in the log-law region inner layer and y^+ is greater than 11 according to the following equation:

$$u_{IB} = u_{PP} - u_\tau \frac{1}{\kappa}\ln\left(\frac{y_{PP}}{y_{IB}}\right), \tag{6}$$

where u_{PP} and u_{IB} are the tangential velocities at the interpolating node and IB node, respectively, and y_{PP} and y_{IB} are the distances from the wall to the interpolating node and IB node, respectively. When y^+ is smaller than 11, the IB node is located in the viscous linear sub-layer, and the tangential velocity at the IB node is determined as:

$$u_{IB} = \rho y_{IB} u_\tau^2 \big/ \mu. \tag{7}$$

The normal velocity is calculated by quadratic interpolation as:

$$u_{n,IB} = u_{n,PP}\left(\frac{y_{IB}^2}{y_{PP}^2}\right). \tag{8}$$

The eddy viscosity ν_t, at the IB nodes is calculated using a mixing-length eddy viscosity model as [28].

$$\nu_t = \kappa u_\tau y_{IB}\left(1 - e^{-\rho y_{IB} u_\tau/(19\mu)}\right)^2, \tag{9}$$

The predecessor of this code adopted analytic functions to define the LS function which can only express solid boundaries with relatively simple shapes, such like circular cylinder, fish body and airfoil [31]. It is challenge to apply that method to generate 3D structures with more complex geometries. In this paper, an unstructured triangular surface mesh in the stereolithography (STL) format is utilized to discretize arbitrary solid bodies. Here we utilized this format file to construct a LS field.

For the LS-based IB method, the LS function is only used to capture the fluid-solid interface and calculate the normal vectors at the projected nodes of IB nodes which are located on the wall boundary. This indicates that only computational nodes near the fluid-solid interface need to be calculated accurately. For nodes in other locations, only the sign should be correct for identifying fluid and solid nodes and the value is not crucial. In Fig. 2, a 2D sketch about the method to construct a LS field is shown. The surface of a 3D body is discretized by triangles, and the surface of a 2D body can be discretized by segments, which are denoted by the red segments in the figure. Only LS function values on the solid square nodes as a neighborhood zone nodes of fluid solid interface are calculated accurately, the other nodes denoted by hollow squares are assigned a value. The overall procedure to construct the LS function field is summarized as the following steps.

1) The solid squares nodes are identified by a small local search circle (sphere for 3D case) of radius r centered at each computational nodes. The radius r is determined by,

$$r \geq \sqrt{\left(2\sqrt{2}\,max(\triangle x, \triangle y)\right)^2 + l_{max}^2} \tag{10}$$

for 2D case, and

$$r \geq \sqrt{\left(2\sqrt{3}\,max(\triangle x, \triangle y, \triangle z)\right)^2 + l_{max}^2} \tag{11}$$

for 3D case. Where $\triangle x, \triangle y, \triangle z$ is the grid size in x-, y-, and z-direction, respectively, and l_{max} is the length of the longest edge of the unstructured mesh triangles. For two-layer computational nodes which are in the immediate vicinity of the fluid-solid interface, this inequation ensures at least one segment (triangle) within its local search circle (sphere). It is observed that all IB nodes lie in this neighborhood zone.

2) Calculate the distance between neighborhood zone node and all segments (triangles) within the local search circle (sphere), and select the smallest one as the distance to the solid body for this

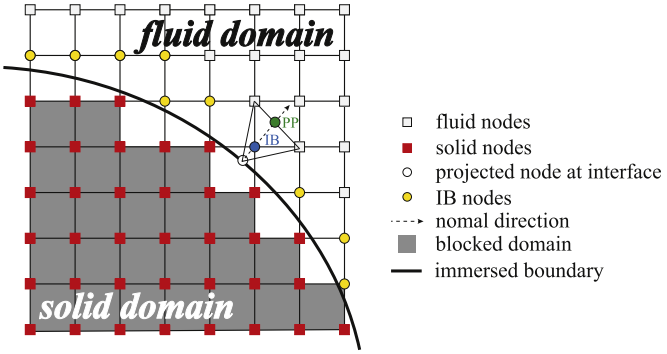

Fig. 1. 2D schematic of level-set based immersed boundary on a Cartesian background grid.

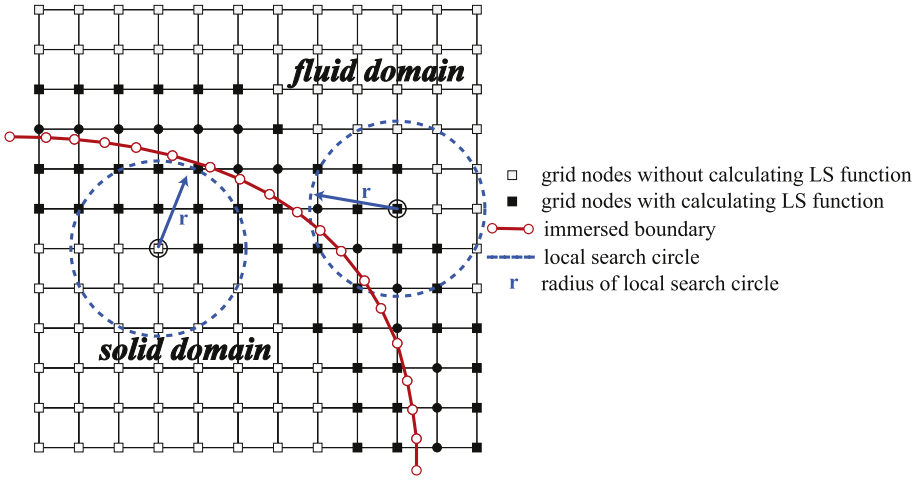

Fig. 2. 2D schematic of the identifying algorithm of nodes in a small local region near the immersed boundary for calculating the distance.

node. The barycentric coordinates formula for calculating the distance between point and triangle for a 3D case is as follows,

$$\alpha \cdot \boldsymbol{v}_1 + \beta \cdot \boldsymbol{v}_2 + \gamma \cdot \boldsymbol{v}_3 = p_0 \tag{12}$$

where $\boldsymbol{v}_1, \boldsymbol{v}_2, \boldsymbol{v}_3$ is the positon vector of each three vertex node of each triangle in unstructured grid, respectively, p_0 is the normal projected point in triangle from the computational node p, and α, β, γ are coefficients. The equations are solved to obtain α, β and γ. If p_0 lies inside the triangle, all components of its barycentric coordinates (α, β, γ) must lie in the interval [0,1]. If not, it indicate that the point p_0 is outside the triangle and the point in the triangle with minimum distance to p lies on one vertex or one edge of the triangle. The criteria based on the sign of α, β and γ is given, i) If the only positive one is α, β or γ, the closest point to p located on the triangle is the node $\boldsymbol{v}_1$, $\boldsymbol{v}_2$ or $\boldsymbol{v}_3$, respectively. ii) If only the only negative is α, β or γ, and the other two are positive, the closest point to p located on the triangle is the edge between $\boldsymbol{v}_2$ and $\boldsymbol{v}_3$, $\boldsymbol{v}_1$ and $\boldsymbol{v}_3$, or $\boldsymbol{v}_1$ and $\boldsymbol{v}_2$, respectively. It is worth-mentioning that coordinates of α, β and γ should not be zero generally, which signifies the singularity. For example, if the precision of coordinates of triangle nodes is too low, ray may go across the edge or node of triangle and singularity occurs in the algorithm.

3) After all neighborhood zone nodes obtain the distance to the solid bodies, directly assign a positive value to other computational nodes including fluid nodes and solid nodes.
4) Identify each computational node if it is located in solid domain or fluid domain. A ray tracing method is utilized to classify fluid and solid computational nodes [34]. A random ray starts from a computational node and the total number of intersections between the ray and unstructured mesh is recorded. The computational node is located inside the solid bodies when the number is odd and outside when the number is even.

3. Setup of the simulation

The discrete STL unstructured mesh is used to assist capturing the geometry of the axial-flow pump in the IB method, which is shown in Fig. 3. The computational domain is shown in Fig. 4(a), and the pump unit in a vertical section across the centerline are illustrated in Fig. 4(b), which r is the distance in the radius direction from the centerline. This simplified horizontal axial-flow pump device consists of an inlet pipe, inlet guide vanes, an impeller (pump rotor), outlet guide vanes, a main shaft and an outlet pipe. The parameters of the pump are shown in Table 1, where D is the inlet and outlet pipe diameter, D_i is the impeller diameter, D_{iin} and D_{iout} are the inlet and outlet diameters of impeller, respectively. H_d is the designed head, δ is the blade tip clearance, Q_d is the designed flow-rate, N_i is the inlet guide vane number, N_o is the outlet guide vane number, N_b is the impeller blade number, ω is the impeller rotating speed, and T is the impeller rotating period. The condition of the pump working with Q_d is defined as designed flow-rate working condition $Q = 1.0Q_{beq}$. The computational domain is set to $6D \times 1.1D \times 1.1D$ in the x-, y-, z-directions, respectively. The streamwise center of the impeller is placed at $x/D = 2.85$.

In LES, when the grid is refined to the Kolmogorov scale, the subgrid-scale stress approaches zero and the simulation converges to DNS. Therefore, it is theoretically infeasible to conduct LES that is fully converged. Here, we added a table of water head and efficiency to show that the present LES is approximately converged, as shown in Table 2. It shows that the water head and efficiency errors under the designed working condition become small when the number of grid points reaches 37.3 million. Owing to the consideration of computational cost, 59 million grid points are the largest we could afford with the computational resources available. Meanwhile, our results are in good agreement with experiment data, indicating that our results are reliable. According to previous studies, such as Antonio Posa et al. [20] using 28 million grid points and Chirag Trivedi et al. [43] using 72 million grid points, the present grid resolution is sufficient to conduct LES. Base on the above considerations, we believe that the grid of the present simulations meets the requirement of LES. Therefore, the number of grid points is set to $1024 \times 240 \times 240$ in the x-, y-, z-directions, respectively. The grid is clustered around the pump for $2.25D < x < 3.45D$, $0.05D < y < 1.05D$ and $0.05D < z < 1.05D$. In this domain, the grid size is $0.0025D$ in x-direction and $0.0042D$ in y-, and z-directions. Outside the refined domain, the grid is stretched to the boundaries in the x-, y-, and z-directions. The Dirichlet velocity inlet and convective outlet boundary conditions are applied in the x-direction. The inflow is exported from a precursor simulation of a fully developed turbulent pipe flow without the presence of the pump. The no-slip boundary condition of the pipe wall is enforced by the IB method. Thus, the flow is driven by the rotating impeller from the low water level to the high water level. By running each case with a constant CFL number which equals to 0.8, we found the time steps are between 3.86×10^{-5}s and 1.55×10^{-4}s. With the consideration of further phase-averaging and other post-

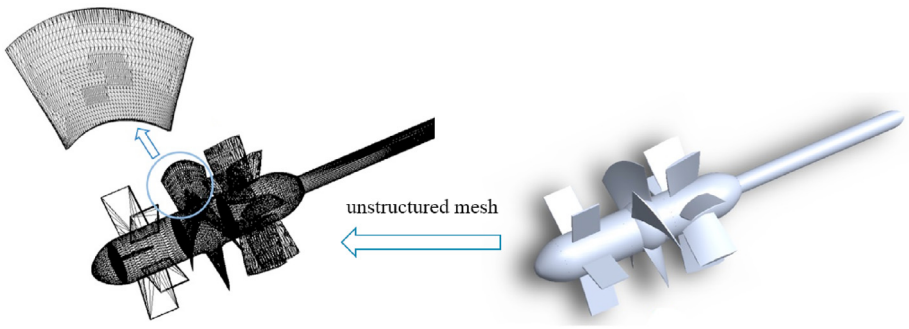

Fig. 3. Discrete unstructured mesh of a complex axial-flow pump expressed in the STL format.

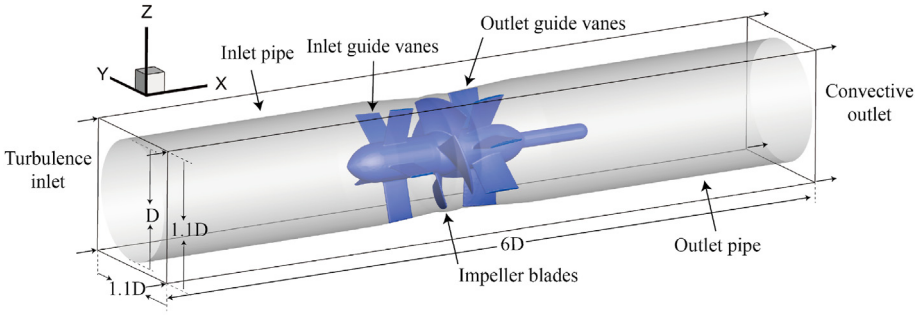

(a) Components and boundary conditions of the axial-flow pump.

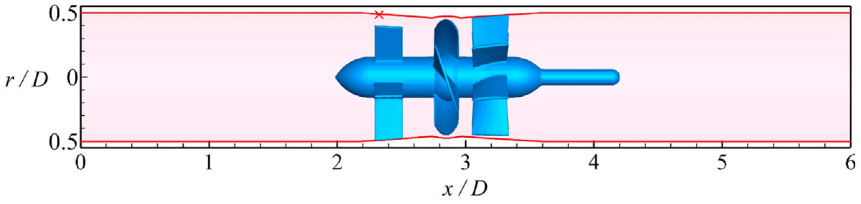

(b) Illustration of the pump unit in the vertical section across the centerline.

Fig. 4. Sketch of an axial-flow pump simulation setup.

Table 1
Parameters of the horizontal axial-flow pump.

D	D_i	D_{iin}/D_{iout}	H_d	δ	Q_d	N_i	N_o	N_b	ω	T
1.8 m	1.7 m	1.6 m	2.2 m	20 mm	10 m^3/s	5	4	7	250 r/min	0.24 s

Table 2
Errors of lifted head and efficiency of different grid schemes.

Grid scheme	Grid number	Lifted head	Head error	Efficiency	Efficiency error
600*128*128	9.8 million	1.787 m	/	51.64%	/
600*192*192	22.1 million	1.965 m	9.1%	60.38%	14%
800*216*216	37.3 million	2.077 m	5.4%	66.99%	9.9%
896*224*224	45.0 million	2.087 m	0.48%	67.31%	0.39%
1024*240*240	59.0 million	2.081 m	0.6%	67.12%	0.19%

processing, the time step is set to a constant value 2×10^{-5}s, in which the impeller rotates by 0.03°. The total time of the simulation is 40 impeller rotating periods. All simulations were conducted on 768 cores of 2.8 GHz Intel™ Xeon X5560 processors with the parallelization achieved by using the MPI. Each case costed approximately 20 days. Computational resources were provided by the University of Minnesota Supercomputing Institute.

4. Validation

Fig. 5 shows a comparison of the lifted water head H and pump hydraulic efficiency η obtained from the present simulation and experimental results. The experiment data is provide by Hitachi Pump Manufacture (Wuxi) Co. Ltd. The largest errors of H and η are found under the low flow-rate working condition, which are approximately 8% and 4%, respectively. The errors under the designed working condition is approximately 5% and 2%, respectively. As the flow-rate increases and the adverse pressure gradient decreases, the simulation result becomes closer to the experimental result.

5. Results

Fig. 6 shows the mean streamwise velocity U at several streamwise locations under the designed flow-rate working condition $Q = 1.0Q_{beq}$. The fully developed incoming turbulent flow is present at $x/D = 1.0$. When the area of the cross section decreases at the impeller inlet, $x/D = 2.7$, the streamwise velocity U increases on average. It increases the most at $x/D = 3.0$ in the wake of the impeller and later decreases at $x/D = 3.4$ due to the expansion of the pipe. Fig. 7 compares the profiles of U at $x/D = 3.0$ under different flow-rate working conditions. The velocity loss near the endwall caused by impeller blade tip leakage (BTL) is significant under the low flow-rate working condition $Q = 0.8Q_{beq}$ and $Q = 0.9Q_{beq}$. The velocity loss becomes less significant as the flow-rate increases, indicating that the effect of the BTL flow is weakened.

Fig. 8 further compares the mean streamwise velocity in a vertical section across the centerline under three different flow-rate working conditions, $Q = 0.8Q_{beq}$, $Q = 1.0Q_{beq}$, and $Q = 1.2Q_{beq}$. The BTL is evident and a low-velocity zone appears behind the outlet guide vanes under the small flow-rate working condition $Q = 0.8Q_{beq}$. Under larger flow-rate working conditions, the BTL flow is weakened and the low-velocity zone is not observed. The BTL adverse velocity decreases as the flow-rate increases. It is known that the adverse velocity is driven by an adverse pressure gradient near the blade tip [7,44].

To further understand the relationship between the adverse pressure gradient and tip leakage flow (TLF) of the mean streamwise flow, the flow field near the blade tip is shown in Fig. 9, which plots the pressure distribution at the vertical section across the centerline and the turbulent kinetic energy (TKE) k distribution at $x/D = 2.85$ (yz-section) under different flow-rate working conditions. The blade rotates in positive x-direction as shown in Fig. 9(a). Under the low flow-rate working condition $Q = 0.8Q_{beq}$, the TLF forms a vortex at the suction side of the blade, resulting in a low-pressure zone there. The low-pressure zone intensifies the adverse pressure gradient near the tip. The TKE magnitude is high at the suction side of the blades due to the TLF and the vortex, as shown in the section $x/D = 2.85$. The vortex and low-pressure zone at the suction side of the blade weaken under the designed flow-rate working condition $Q = 1.0Q_{beq}$ as shown in Fig. 9(b) and disappear under the high flow-rate working condition $Q = 1.2Q_{beq}$ as shown in Fig. 9(c). These results indicate that the TLF, vortex intensity, and turbulence intensity near the tip all weaken as the flow-rate increases.

The strong turbulent motions occur not only near the impeller tip but also near the outlet guide vanes. Fig. 10 shows the radial vorticity ω_r at the mid-span circumferential section $r/D = 0.3$ around one blade of the outlet guide vanes under different flow-rate working conditions. Because the streamwise velocity increases from the low flow-rate working condition to the high flow-rate working condition, the angle of attack (the angle from the chord to the direction of relative velocity to the blade with the clockwise direction being negative) also decreases. Under the

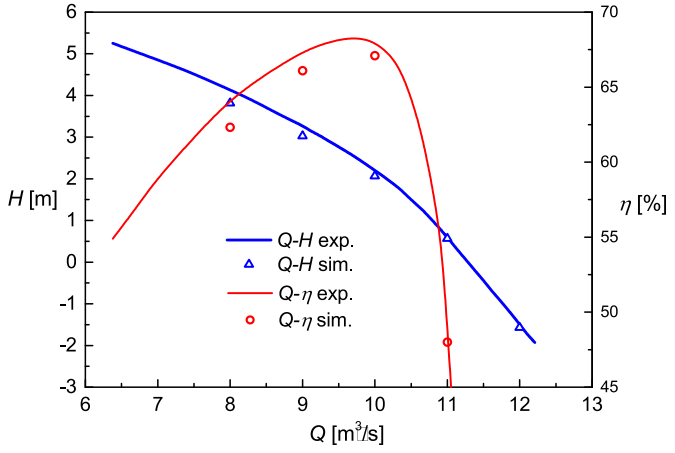

Fig. 5. Comparison of flow-rate Q vs lifted water head H between experiment and simulation.

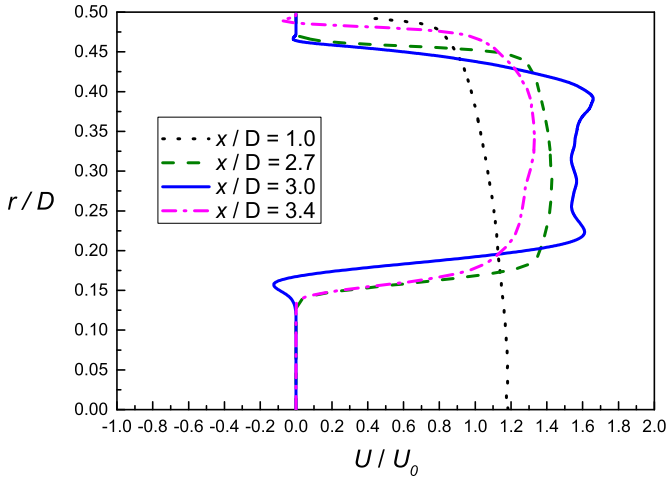

Fig. 6. Mean streamwise velocity U under the designed flow-rate working condition$Q = 1.0Q_{beq}$.

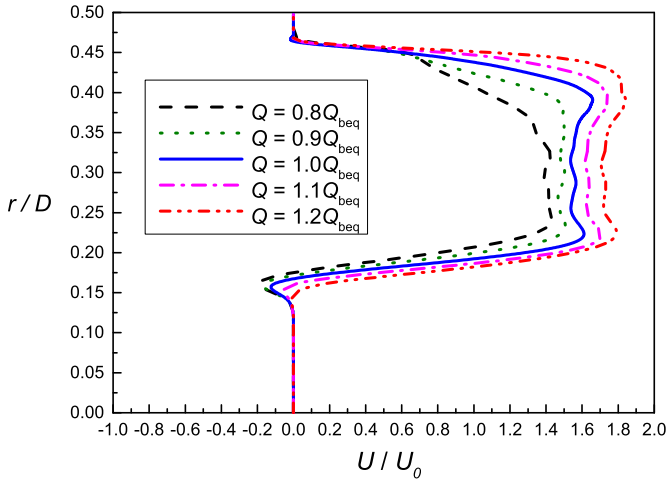

Fig. 7. Mean streamwise velocity U at $x/D = 3.0$ under different flow-rate working conditions.

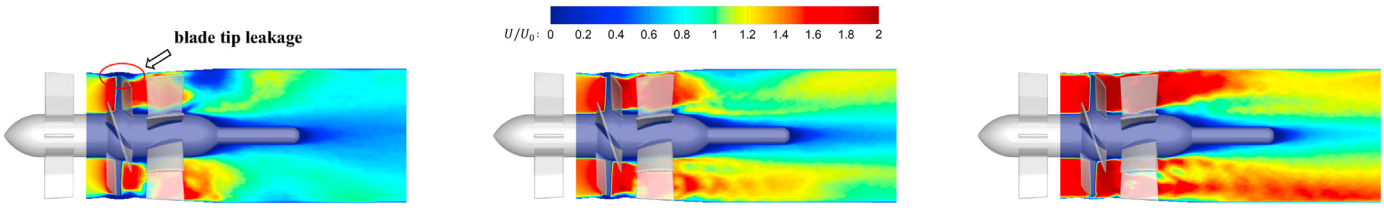

(a) $Q = 0.8Q_{beq}$ (b) $Q = 1.0Q_{beq}$ (c) $Q = 1.2Q_{beq}$

Fig. 8. Mean streamwise velocity distribution at the vertical section across the centerline under different flow-rate working conditions.

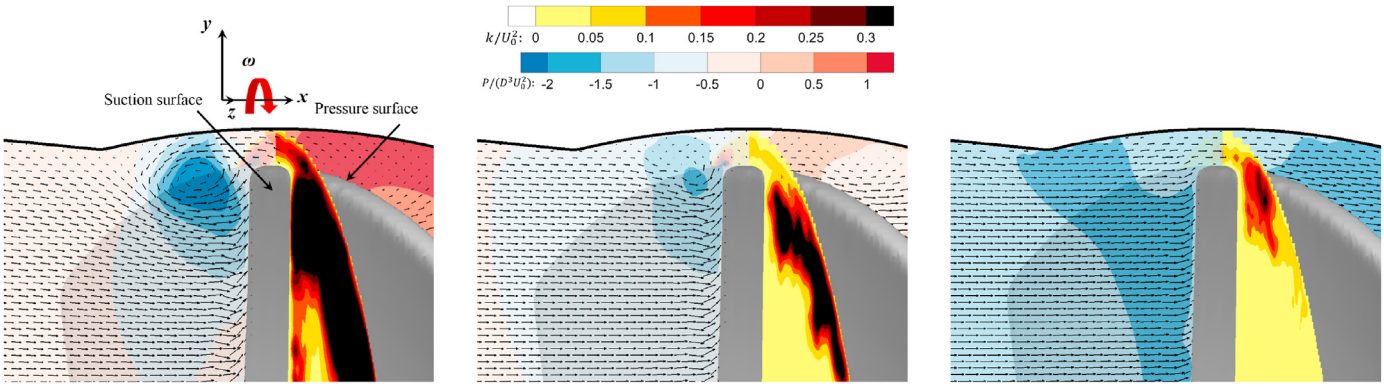

(a) $Q = 0.8Q_{beq}$ (b) $Q = 1.0Q_{beq}$ (c) $Q = 1.2Q_{beq}$

Fig. 9. Pressure distribution at the vertical section across the centerline and TKE distribution at $x/D = 2.85$ (yz-section) under different flow-rate working conditions.

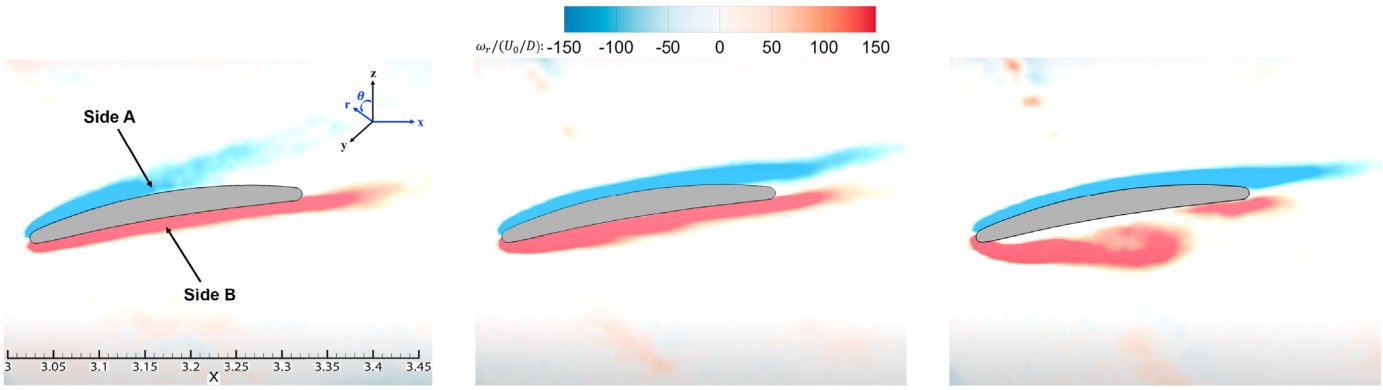

(a) $Q = 0.8Q_{beq}$ (b) $Q = 1.0Q_{beq}$ (c) $Q = 1.2Q_{beq}$

Fig. 10. Radial vorticity at the midspan circumferential section around one blade of the outlet guide vanes under different flow-rate working conditions.

designed flow-rate working condition $Q = 1.0Q_{beq}$, as shown in Fig. 10(b), the absolute value of vorticity is large. The flow is smooth near the boundary of the outlet guide vane and there is no flow separation. Under the low flow-rate working condition $Q = 0.8Q_{beq}$, the angle of attack is negative, and the vorticity is small in the area close to the tail of the upper surface of the outlet guide vane, which means that the boundary layer detaches from the upper surface into the wake [45], as shown in Fig. 10(a). Under the high flow-rate working condition $Q = 1.2Q_{beq}$, as shown in Fig. 10(c), the angle of attack is positive, and the vorticity in the area close to the tail of the bottom surface of the outlet guide vane is small. As a result, the boundary layer at the bottom surface is unsteady and detached.

To further study the flow separation over the outlet guide vane, Fig. 11 shows the radial vorticity in the cross-stream plane located at $x/D = 3.4$ under different flow-rate working conditions. The radial vorticity shows the radial location over the outlet guide vanes where flow separation takes place. From Fig. 11(a), it is seen that under the low flow-rate working condition $Q = 0.8Q_{beq}$, the radial vorticity near the tip of side A is relatively small, indicating the separation occurs there. Under the high flow-rate working condition $Q = 1.2Q_{beq}$ shown in Fig. 11(c), flow separation takes places near the blade root of side B, where the radial vorticity is relatively small. Therefore, it can be deduced that the turbulence is intense in the tip and root area under small and high flow-rate working conditions, respectively. This feature is further demonstrated below in Fig. 15(b).

Thus far, we have studied the TLV structure near the impeller blade and flow separation over the outlet guide vane. In the following content, we further demonstrates the effects of the TLV

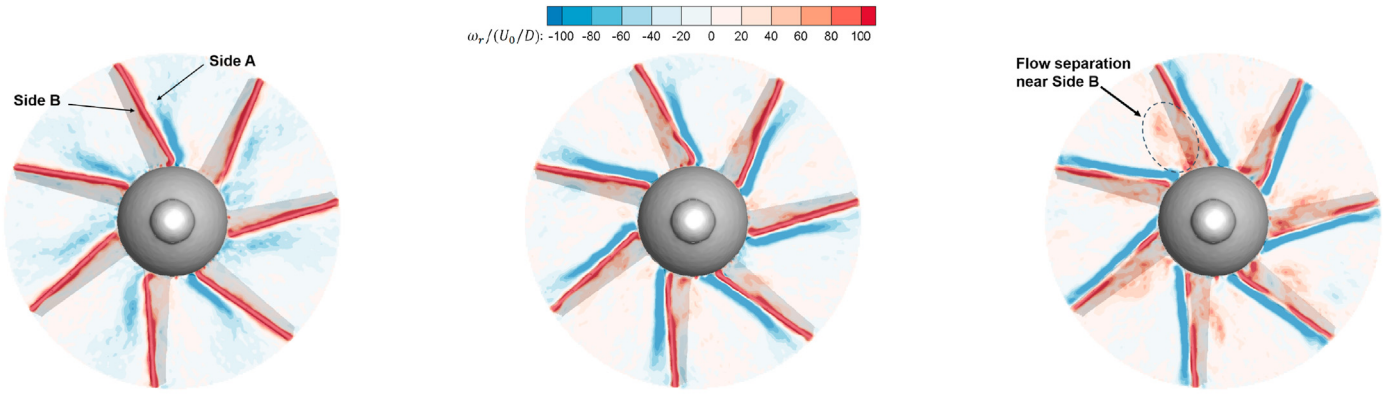

(a) $Q = 0.8Q_{beq}$ (b) $Q = 1.0Q_{beq}$ (c) $Q = 1.2Q_{beq}$

Fig. 11. Radial vorticity at the $x/D = 3.4$ (yz-section) under different flow-rate working conditions.

and flow separation on the turbulence statistics and the pump working efficiency under various flow-rate working conditions. Fig. 12 shows the TKE distribution in the circumferential section located at $r/D = 0.3$ under different flow-rate working conditions. By contrasting the results at three different flow-rate working conditions shown in Fig. 12, it is evident that compared with the designed flow-rate working condition $Q = 1.0Q_{beq}$, the TKE near the outlet guide vanes is relatively high under the low flow-rate working condition $Q = 0.8Q_{beq}$ and high flow-rate working condition $Q = 1.2Q_{beq}$. The distribution of high TKE is consistent with the flow separation phenomenon discussed above because the zones of high TKE values often correspond to flow detachment [46].

To illustrate the statistical characteristics of the turbulence, Fig. 13 plots the total TKE, k_T, integrated over the entire computational domain. The integral TKE k_T is the lowest under the designed flow-rate working condition $Q = 1.0Q_{beq}$. The more the flow-rate departs from the designed flow-rate working condition, the higher the total TKE k_T is.

Fig. 14 shows the TKE $k_x = \frac{1}{2}\langle u_i' u_i' \rangle_{r\theta t}$ as a function of the x-location under different flow-rate working conditions, where $\langle \bullet \rangle_{r\theta t}$ represents averaging over the radial direction, circumferential direction, and time. We divide the variations of k_x into three zones. In zone I, the TKE of the inflow is relatively low, and the TKE starts to increase slightly from $x/D = 2.5$, the exit of the inlet guide vanes. In zone II, the flow enters the rotating impeller at approximately $x/D = 2.7$, and the primary peak of k_x occurs around $x/D = 3.0$. The magnitude of the primary peak of TKE is larger under the low flow-rate working condition $Q = 0.8Q_{beq}$ than under the designed flow-rate working condition and high flow-rate working conditions. Meanwhile, the value of the primary peak of k_x under the high flow-rate working condition $Q = 1.2Q_{beq}$ is close to that under the designed flow-rate working condition $Q = 1.0Q_{beq}$. This is because

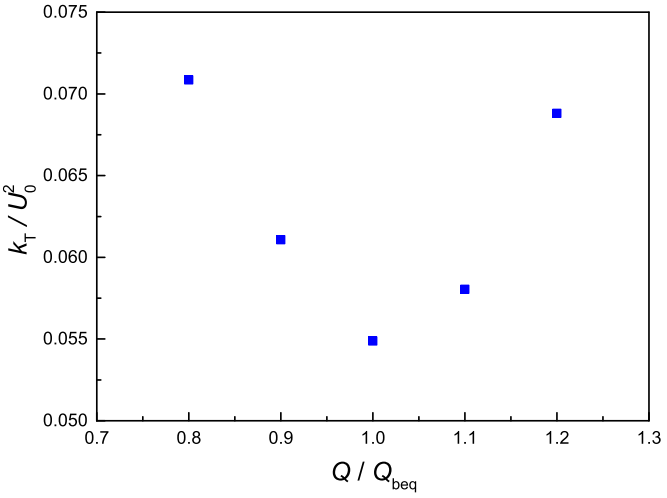

Fig. 13. Integral TKE under five different flow-rate working conditions.

the high TKE in zone II is mainly induced by the TLV formed due to the local adverse pressure gradient near the impeller blade tip, which becomes larger as the flow-rate decreased. This result is consistent with the high TKE around impeller blade tip shown in Fig. 9. In zone III, a secondary peak occurs in the profile of k_x around $x/D = 3.5$, the wake area of the outlet guide vanes. Among the five flow-rate working conditions, the magnitude of k_x is the lowest under the designed flow-rate working condition $Q = 1.0Q_{beq}$, and the more the flow-rate departs from the designed flow-rate working condition $Q = 1.0Q_{beq}$, the larger the value of k_x is. This is because the high TKE in zone III is mainly induced by the flow

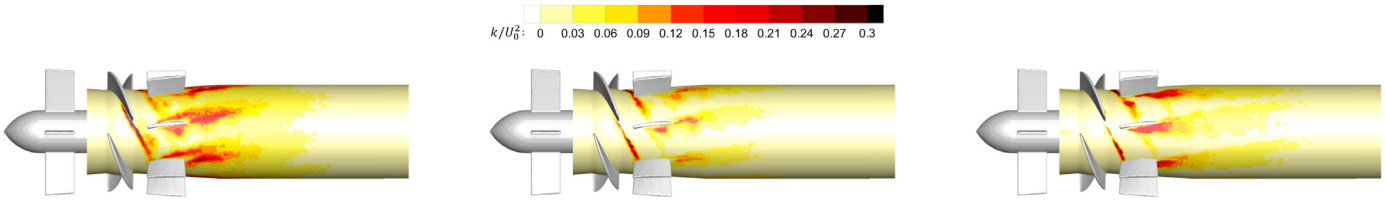

(a) $Q = 0.8Q_{beq}$ (b) $Q = 1.0Q_{beq}$ (c) $Q = 1.2Q_{beq}$

Fig. 12. TKE distribution at the midspan circumferential section under different flow-rate working conditions.

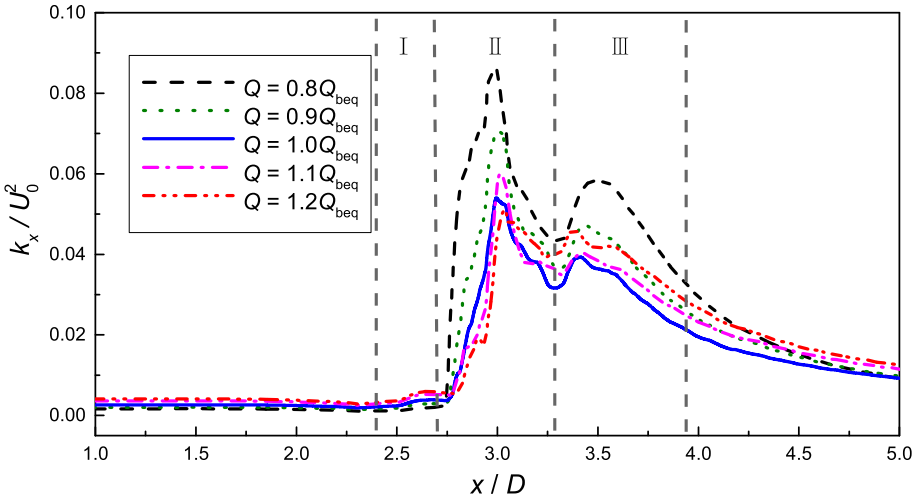

Fig. 14. TKE k_x integrated in the yz-section as a function of the downstream x location under different flow-rate working conditions.

separation over the outlet guide vanes, which is present at both low and high flow-rate working conditions, but is absent under the designed flow-rate working condition. This result is consistent with the high TKE around the outlet guide vanes shown in Fig. 12. To summarize the study of the streamwise distribution of TKE, the first peak of k_x characterizes the strong turbulent motion generated by the TLV at the gap between the impeller blades and casing, and the secondary peak of k_x is mainly induced by the flow separation over the outlet guide vanes.

To further understand the effect of the flow-rate working condition on the distribution of TKE, we examine the radial profile of TKE $k_r = \langle u_i' u_i' \rangle_{\theta t}$, where $\langle \cdot \rangle_{\theta t}$ denote averaging over the circumferential direction and time. Fig. 15 depicts the profiles of k_r at two specific streamwise locations, $x/D = 3.0$ and 3.4, where the primary and secondary peaks of k_x occur (Fig. 14). Fig. 15(a) shows that at $x/D = 3.0$, high k_r occurs near the case. In this region, the magnitude of k_r increases as the flow-rate decreases. This indicates that the high TKE k_x in Fig. 14 at $x/D = 3.0$ is composed of high TKE k_r near the casing side. Collocated with the TLV, it demonstrates that the high TKE is mainly caused by the TLV. Fig. 15(b) shows that at $x/D = 3.4$, high TKE occurs near the casing side and near the hub in the low and high flow-rate working conditions, respectively. This high TKE region is consistent with the flow separation region shown by the radial vorticity in Figs. 11 and 12.

Figs. 16 and 17 show the streamwise turbulence production P and turbulence dissipation ε under different flow-rate working conditions. The TKE equation can be expressed as:

$$\frac{Dk}{Dt} + \nabla \cdot T' = P - \varepsilon, \tag{13}$$

where k is the TKE, $\nabla \cdot T'$ is the diffusion of TKE, $P = -\overline{u_i' u_j'} \frac{\partial \overline{u_i}}{\partial u_j}$ is the energy production, and $\varepsilon = \nu \overline{\frac{\partial u_i'}{\partial u_j} \frac{\partial' u_i}{\partial u_j}}$ is the energy dissipation. The energy production represents the energy transfer from mean flow to velocity fluctuations, which is the main source for sustaining the turbulent motions. The role of the energy dissipation is to consume the TKE by viscosity. From the physical meaning of the production and dissipation of TKE, it is understood that these two processes lead to the loss the machine efficiency. Therefore, the

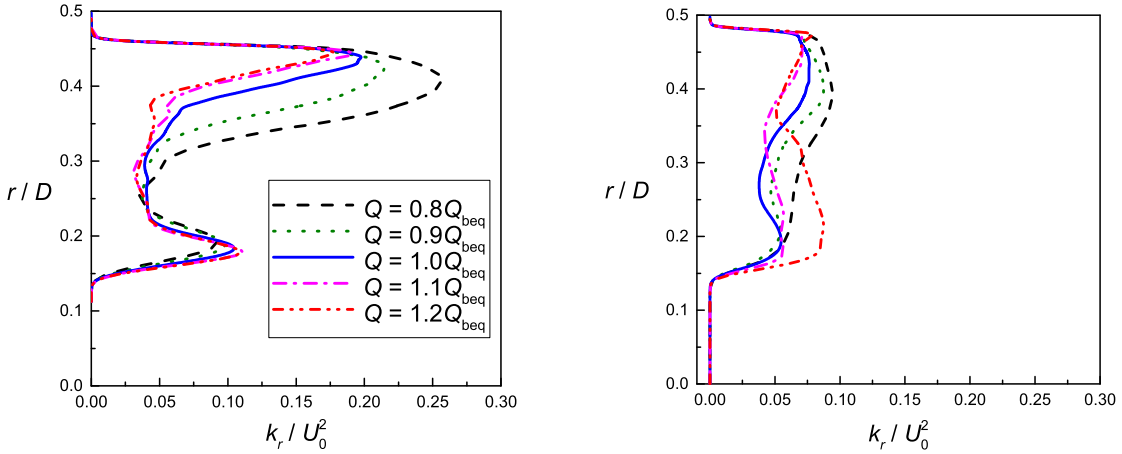

(a) TKE k_r of impeller wake at $x/D = 3.0$

(b) TKE k_r of outlet guide vanes wake at $x/D = 3.4$

Fig. 15. TKE k_r integrated in the circumferential direction as a function of radial location under different flow-rate working conditions.

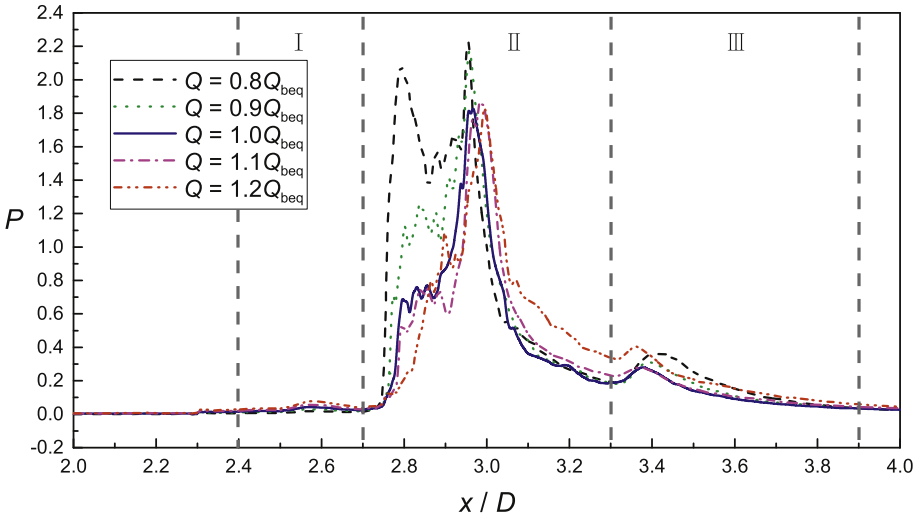

Fig. 16. Turbulence production under different flow-rate working conditions.

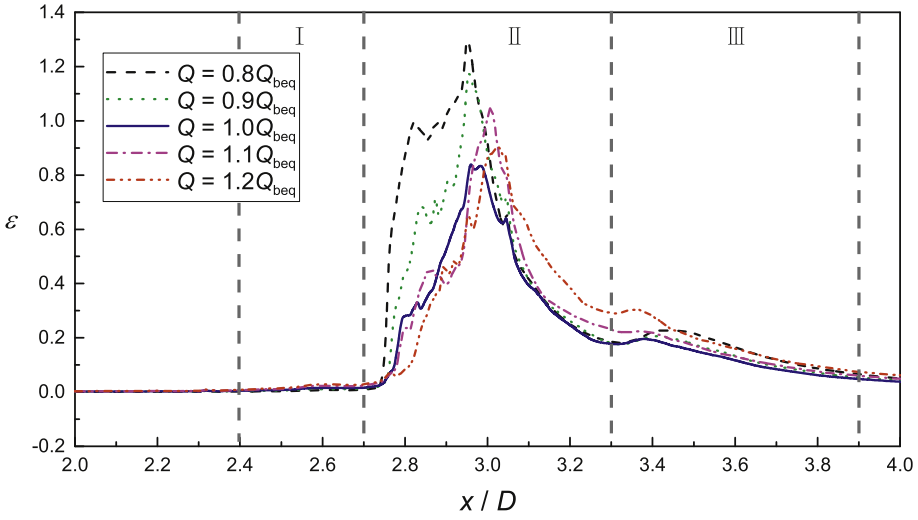

Fig. 17. Turbulence dissipation under different flow-rate working conditions.

investigations of the energy production and dissipation provide insights into the flow physics, which are useful for the design and modification of the axial-flow pump.

Figs. 16 and 17 show that, in zone I, similar to TKE, the values of P and ε start to increase slightly from $x/D = 2.5$, the exit of the inlet guide vanes. In zone II, the magnitudes of P and ε are much larger than those in zone I, because the flow is highly disturbed by the rotating impeller blades from approximately $x/D = 2.7$ to $x/D = 3.0$. The values of P and ε both increase as the flow-rate decreases, and they are evidently larger under low flow-rate working conditions than under other flow-rate working conditions. From approximately $x/D = 3.0$ to $x/D = 3.3$, which is the streamwise location of the outlet guide vanes, P and ε under high flow-rate working conditions become high in the five flow-rate working conditions in the area of the outlet guide vanes. This is due to the larger convection and flow separation at the high velocity of the high flow-rate. In zone III, at $x/D = 3.4$, the trailing edge of the outlet guide vanes, the values of P and ε under both low flow-rate working condition $Q = 0.8Q_{beq}$ and high flow-rate working condition $Q = 1.2Q_{beq}$ are larger than those under the designed flow-rate working condition. As discussed above, the flow separation dominates the larger magnitude of TKE production and dissipation at off-designed flow-rate working conditions.

6. Conclusions

In this study, we developed a novel level-set function based immersed boundary method to simulate a geometrically complex pump. The LES of an axial-flow pump under five flow-rate working conditions is conducted. The simulation results of energy efficiency are compared with the data acquired from experiments and the results are consistent with the data acquired from experiments. The results can be summarized below.

- The LES results reveal that among the five different flow-rate working conditions, the integral TKE reaches its minimum value under the designed flow-rate working condition. The more the flow-rate departs from the designed flow-rate working condition, the higher the total TKE k_T is.
- Tip leakage flow and flow separation are closely connected with high TKE magnitude under the off-designed flow-rate working conditions. The tip leakage flow plays a leading role in

generating high TKE at the tip of the impeller blades under low flow-rate working conditions, and flow separation is responsible for the high TKE in the wake of the outlet guide vanes under both low and high flow-rate working conditions.

- The tip leakage flow occurs due to the adverse pressure gradient in the gap between the impeller blade tip and the shell of the pump. Visualization of the flow field shows that a vortex occurs on the suction side of the impeller blade, which leads to a low-pressure zone there. As the flow-rate decreases, the adverse pressure gradient near the impeller tip becomes larger, resulting in a larger magnitude of TKE. The flow separation over the outlet guide vanes under the off-designed flow-rate working conditions leads to the detachment of vortices from the two sides of a guide vane into the wake, causing a high TKE magnitude in the wake flow.

CRediT authorship contribution statement

Kan Kan: Conceptualization, Methodology, Software, Validation, Formal analysis, Writing - original draft. **Zixuan Yang:** Methodology, Software, Writing - original draft, Writing - review & editing. **Pin Lyu:** Methodology, Writing - original draft, Writing - review & editing. **Yuan Zheng:** Validation, Writing - review & editing, Supervision. **Lian Shen:** Conceptualization, Methodology, Formal analysis, Resources, Supervision.

Declaration of competing interest

The author(s) declare no potential conflicts of interest with respect to the research, authorship, and/or publication of this article.

Acknowledgement

The study was supported by the National Natural Science Foundation of China (52009033), the Natural Science Foundation of Jiangsu Province (BK20200509) and the Fundamental Research Funds for the Central Universities (B210202066).

References

[1] C.E. Brennen, A review of the dynamics of cavitating pumps, J. Fluid Eng. 135 (6) (2013).
[2] D.J. Laser, J.G. Santiago, A review of micropumps, J. Micromech. Microeng. 14 (6) (2004) R35.
[3] W.C. Zierke, W.A. Straka, Flow visualization and the three-dimensional flow in an axial-flow pump, J. Propul. Power 12 (2) (1996) 250–259.
[4] W.C. Zierke, W.A. Straka, P.D. Taylor, The High Reynolds Number Flow through an Axial-Flow Pump. Technical Report, Pennsylvania State University/Applied Research Lab, 1993.
[5] W.C. Zierke, W.A. Straka, P.D. Taylor, An experimental investigation of the flow through an axial-flow pump, J. Fluid Eng. 117 (3) (1995) 485–490.
[6] O. Uzol, Y.C. Chow, J. Katz, C. Meneveau, Unobstructed particle image velocimetry measurements within an axial turbo-pump using liquid and blades with matched refractive indices, Exp. Fluid 33 (6) (2002) 909–919.
[7] Desheng Zhang, Weidong Shi, Bart van Esch, Lei Shi, Michel Dubuisson, Numerical and experimental investigation of tip leakage vortex trajectory and dynamics in an axial flow pump, Comput. Fluids 112 (2015) 61–71.
[8] Yabin Liu, Lei Tan, Spatial–temporal evolution of tip leakage vortex in a mixed-flow pump with tip clearance, J. Fluid Eng. 141 (8) (2019).
[9] Yadong Han, Lei Tan, Dynamic mode decomposition and reconstruction of tip leakage vortex in a mixed flow pump as turbine at pump mode, Renew. Energy 155 (2020) 725–734.
[10] Xijie Song, Chao Liu, Experimental investigation of floor-attached vortex effects on the pressure pulsation at the bottom of the axial flow pump sump, Renew. Energy 145 (2020) 2327–2336.
[11] Felix Muggli, Holbein Peter, Philippe Dupont, CFD calculation of a mixed flow pump characteristic from shutoff to maximum flow, J. Fluid Eng. 124 (3) (2002) 798–802.
[12] Chao Liu, Yang Fan, Yan Jin, Hua Yang, Flow characteristics of high-efficient axial flow pump system, in: ASME Power Conference, vol. 56604, American Society of Mechanical Engineers, 2015. V001T12A005.
[13] Yang Fan, Hao-ru Zhao, Chao Liu, Improvement of the efficiency of the axial-flow pump at part loads due to installing outlet guide vanes mechanism, Math. Probl Eng. (2016) 2016.
[14] J. Pei, SQ Yuan Hj Dohmen, F.K. Benra, Investigation of unsteady flow-induced impeller oscillations of a single-blade pump under off-design conditions, J. Fluid Struct. 35 (2012) 89–104.
[15] Jianjun Zhu, Hattan Banjar, Zhenyan Xia, Hong-Quan Zhang, CFD simulation and experimental study of oil viscosity effect on multi-stage electrical submersible pump (ESP) performance, J. Petrol. Sci. Eng. 146 (2016) 735–745.
[16] M.H. Shojaeefard, M. Tahani, M.B. Ehghaghi, Fallahian Ma, M. Beglari, Numerical study of the effects of some geometric characteristics of a centrifugal pump impeller that pumps a viscous fluid, Comput. Fluids 60 (2012) 61–70.
[17] Thiago Sirino, Henrique Stel, Rigoberto Morales, Numerical study of the influence of viscosity on the performance of an electrical submersible pump, in: ASME 2013 Fluids Engineering Division Summer Meeting, American Society of Mechanical Engineers, 2013. FEDSM2013–16374, V01BT10A026.
[18] Henrique Stel, Thiago Sirino, P.R. Prohmann, Francisco Ponce, Sergio Chiva, Rigoberto Morales, CFD investigation of the effect of viscosity on a three-stage electric submersible pump, in: ASME 2014 4th Joint US-European Fluids Engineering Division Summer Meeting Collocated with the ASME 2014 12th International Conference on Nanochannels, Microchannels, and Minichannels, American Society of Mechanical Engineers, 2014. FEDSM2014–21538, V01BT10A029.
[19] A. Lucius, G. Brenner, Unsteady CFD simulations of a pump in part load conditions using scale-adaptive simulation, Int. J. Heat Fluid Flow 31 (6) (2010) 1113–1118.
[20] Antonio Posa, Antonio Lippolis, Roberto Verzicco, Balaras Elias, Large-eddy simulations in mixed-flow pumps using an immersed-boundary method, Comput. Fluids 47 (1) (2011) 33–43.
[21] R.K. Byskov, C.B. Jacobsen, Nicholas Pedersen, Flow in a centrifugal pump impeller at design and off-design conditions–part II: large eddy simulations, J. Fluid Eng. 125 (1) (2003) 73–83.
[22] C. Kato, M. Kaiho, A. Manabe, An overset finite-element large-eddy simulation method with applications to turbomachinery and aeroacoustics, J. Appl. Mech. 70 (1) (2003) 32–43.
[23] Yoshinobu Yamade, Chisachi Kato, Hayato Shimizu, Takahide Nagahara, Large eddy simulation of internal flow of a mixed-flow pump, in: ASME 2009 Fluids Engineering Division Summer Meeting, American Society of Mechanical Engineers, 2009, pp. 407–416.
[24] Hao Liu, K. Kawachi, A numerical study of insect flight, J. Comput. Phys. 146 (1) (1998) 124–156.
[25] Tony Sheu, Y.H. Chen, Numerical study of flow field induced by a locomotive fish in the moving meshes, Int. J. Numer. Methods Eng. 69 (11) (2007) 2247–2263.
[26] J. Nicolle, J.F. Morissette, A.M. Giroux, Transient CFD simulation of a francis turbine startup, in: IOP Conference Series: Earth and Environmental Science, vol. 15, IOP Publishing, 2012, 062014.
[27] Mehmet Sahin, Kamran Mohseni, An arbitrary Lagrangian–Eulerian formulation for the numerical simulation of flow patterns generated by the hydromedusa aequorea victoria, J. Comput. Phys. 228 (12) (2009) 4588–4605.
[28] Seokkoo Kang, Iman Borazjani, J.A. Colby, Fotis Sotiropoulos, Numerical simulation of 3D flow past a real-life marine hydrokinetic turbine, Adv. Water Resour. 39 (2012) 33–43.
[29] Dionysios Angelidis, Saurabh Chawdhary, Fotis Sotiropoulos, Unstructured Cartesian refinement with sharp interface immersed boundary method for 3D unsteady incompressible flows, J. Comput. Phys. 325 (2016) 272–300.
[30] Saurabh Chawdhary, Dionysios Angelidis, Jonathan Colby, Corren Dean, Lian Shen, Fotis Sotiropoulos, Multi-resolution large-eddy simulation of an array of hydrokinetic turbines in a field-scale river: the Roosevelt Island tidal energy project in New York City, Water Resour. Res. 54 (12) (2018) 10–188.
[31] Zuo Cui, Zixuan Yang, Hongzhou Jiang, Weixi Huang, Lian Shen, A sharp-interface immersed boundary method for simulating incompressible flows with arbitrarily deforming smooth boundaries, Int. J. Comput. Methods 15 (1) (2018) 1750080.
[32] Anvar Gilmanov, Fotis Sotiropoulos, A hybrid Cartesian/immersed boundary method for simulating flows with 3D, geometrically complex, moving bodies, J. Comput. Phys. 207 (2) (2005) 457–492.
[33] E.H. Spanier, Algebraic Topology, 1995. Corrected reprint of the 1966 original.
[34] Iman Borazjani, Ge Liang, Fotis Sotiropoulos, Curvilinear immersed boundary method for simulating fluid-structure interaction with complex 3d rigid bodies, J. Comput. Phys. 227 (16) (2008) 7587–7620.
[35] Smagorinsky Joseph, General circulation experiments with the primitive equations: I. the basic experiment, Mon. Weather Rev. 91 (3) (1963) 99–164.
[36] Massimo Germano, Piomelli Ugo, Parviz Moin, W.H. Cabot, A dynamic subgrid-scale eddy viscosity model, Phys. Fluid. Fluid Dynam. 3 (7) (1991) 1760–1765.
[37] D.K. Lilly, A proposed modification of the Germano subgrid-scale closure method, Phys. Fluid. Fluid Dynam. 4 (3) (1992) 633–635.
[38] Satish Balay, Shrirang Abhyankar, Mark Adams, Jed Brown, Peter Brune, Kris Buschelman, Lisandro Dalcin, Dener Alp, Victor Eijkhout, W. Gropp, et al., Petsc Users Manual, 2019.
[39] Zixuan Yang, Xinhua Lu, Xin Guo, Yi Liu, Lian Shen, Numerical simulation of sediment suspension and transport under plunging breaking waves, Comput. Fluids 158 (2017) 57–71.

[40] Shengbai Xie, Di Yang, Yi Liu, Lian Shen, Simulation-based study of wind loads on semi-submersed object in ocean wave field, Phys. Fluids 28 (1) (2016), 015106.
[41] Sida He, Zixuan Yang, Lian Shen, Numerical study of interactions among air, water, and rigid/flexible solid bodies, Bull. Am. Phys. Soc. 62 (2017).
[42] F. Roman, V. Armenio, J. Fröhlich, A simple wall-layer model for large eddy simulation with immersed boundary method, Phys. Fluids 21 (10) (2009) 101701.
[43] Chirag Trivedi, Ole Gunnar Dahlhaug, Interaction between trailing edge wake and vortex rings in a francis turbine at runaway condition: compressible large eddy simulation, Phys. Fluids 30 (7) (2018), 075101.
[44] R.L. Miorini, Huixuan Wu, Joseph Katz, The internal structure of the tip leakage vortex within the rotor of an axial waterjet pump, J. Turbomach. 134 (3) (2012), 031018.
[45] D.C. Wilcox, Basic Fluid Mechanics, DCW Industries Flintridge, CA, 2000.
[46] Jens Keller, Eduardo Blanco, Ra Barrio, Jorge Parrondo, PIV measurements of the unsteady flow structures in a volute centrifugal pump at a high flow rate, Exp. Fluid 55 (10) (2014) 1820.